

Minimization of phonon-tunneling dissipation in mechanical resonators

Garrett D. Cole,^{1,*} Ignacio Wilson-Rae,^{2,*} Katharina Werbach,¹ Michael R. Vanner,¹ and Markus Aspelmeyer^{1,†}

¹*Faculty of Physics, University of Vienna, Boltzmannngasse 5, A-1090 Vienna, Austria.*

²*Technische Universität München, 85748 Garching, Germany.*

(Dated: October 21, 2021)

Micro- and nanoscale mechanical resonators have recently emerged as ubiquitous devices for use in advanced technological applications, for example in mobile communications and inertial sensors, and as novel tools for fundamental scientific endeavors. Their performance is in many cases limited by the deleterious effects of mechanical damping. Here, we report a significant advancement towards understanding and controlling support-induced losses in generic mechanical resonators. We begin by introducing an efficient numerical solver, based on the “phonon-tunneling” approach, capable of predicting the design-limited damping of high-quality mechanical resonators. Further, through careful device engineering, we isolate support-induced losses and perform the first rigorous experimental test of the strong geometric dependence of this loss mechanism. Our results are in excellent agreement with theory, demonstrating the predictive power of our approach. In combination with recent progress on complementary dissipation mechanisms, our phonon-tunneling solver represents a major step towards accurate prediction of the mechanical quality factor.

Mechanical coupling of a suspended structure to its supports is a fundamental energy loss mechanism in micro- and nanomechanical resonators¹. Referred to variously as clamping² or anchor loss³, this process remains significant even in devices fabricated from high-quality materials operated in vacuum and at cryogenic temperatures, and is in fact unavoidable in any non-levitating system. Although much progress has been made towards the understanding of mechanical dissipation at the micro- and nanoscale^{2,4}, obtaining reliable predictions for the fundamental design-limited quality factor Q remains a major challenge while direct experimental tests are scarce. At the same time, the implementation of high-quality micro- and nanomechanical systems is becoming increasingly important for numerous advanced technological applications in sensing and metrology, with select examples including wireless filters^{3,5}, on-chip clocks⁶, microscopy^{7–10} and molecular-scale mass sensing^{11,12}, and recently for a new generation of macroscopic quantum experiments that involve mesoscopic mechanical structures^{13–20}. Here we introduce a finite-element enabled numerical solver for calculating the support-induced losses of a broad range of low-loss mechanical resonators. We demonstrate the efficacy of this approach via comparison with experimental results from microfabricated devices engineered in order to isolate support-induced losses by allowing for a significant variation in geometry, while keeping other resonator characteristics approximately constant. The efficiency of our solver results from the use of a perturbative scheme that exploits the smallness of the contact area, specifically the recently introduced “phonon-tunneling” approach²¹. This results in a significant simplification over previous approaches and paves the way for CAD-based predictive design of low-loss mechanical resonators.

The origins of mechanical damping in micro- and nanoscale systems have been the subject of numerous studies during the last decades and several relevant mechanisms for the decay of acoustic mechanical exci-

tations, i.e. phonons, have been investigated^{2,4}. These include: (i) fundamental anharmonic effects such as phonon-phonon interactions^{4,22}, thermoelastic damping (TED)^{4,22–25}, and the Akhiezer effect^{4,22}; (ii) viscous or fluidic damping, involving interactions with the surrounding atmosphere or the compression of thin fluidic layers^{26–28}; (iii) materials losses driven by the relaxation of intrinsic or extrinsic defects in the bulk or surface of the resonator^{29–33} for which the most commonly studied model is an environment of two-level fluctuators^{34,35} and (iv) support-induced losses, i.e. the dissipation induced by the unavoidable coupling of the resonator to the substrate^{3,5,36–38}, which corresponds to the radiation of elastic waves into the supports^{21,39–43}. This last mechanism poses a fundamental limit as vibrations of the substrate will always be present.

These various dissipation processes add incoherently such that the reciprocals of the corresponding Q -values satisfy $1/Q_{\text{tot}} = \sum_i 1/Q_i$, where i labels the different mechanisms. Thus, in a realistic setting care must be taken to isolate the contribution under scrutiny. In contrast to all other damping mechanisms (i)-(iii) which exhibit various dependencies with external physical variables such as pressure and temperature, support-induced dissipation is a temperature and scale-independent phenomenon with a strong geometric character that is present in any suspended structure. Moreover, its scale-independence implies that the same analysis can be applied to both micro- and nanoscale devices. We exploit this geometric character in order to isolate the support-induced contribution and obtain a direct experimental test of phonon-tunneling dissipation.

We first introduce our numerical solver, which provides a new technique to efficiently model support-induced losses for a broad class of mechanical structures. Previous approaches have relied on either the direct solution of an elastic wave radiation problem involving the substrate^{39–41,43} or the simulation of a perfectly absorbing artificial boundary^{38,42}, with applications typically lim-

ited to a few specific geometries^{37,38,42,43}. In contrast, our technique represents a substantial simplification in that it reduces the problem to the calculation of a perfectly decoupled resonator mode together with *free* elastic wave propagation through the substrate in the absence of the suspended structure. A key feature of our method is to combine a standard finite-element method (FEM) calculation of the resonator mode together with the use of an extended contact at the support. This allows us to treat complex geometries taking proper account of interference effects between the radiated waves.

In analogy to radiation tunneling in photonics and electron tunneling in low-dimensional structures, we adopt a “phonon tunneling” picture to describe the support-induced losses²¹. In this picture the mechanical resonance of interest, characterized by frequency ω_R , is regarded as a phonon cavity that is weakly coupled to the exterior by a hopping process, whereby the elastic energy leaks out of the resonator through the narrow contact areas from which it is suspended. Within this framework, one can start from the harmonic Hamiltonian associated with the elastic scattering eigenmodes of the entire structure, including the substrate, and derive a quantum model for the Brownian motion experienced by each resonance of the suspended structure.

The corresponding weak tunnel couplings can be obtained to lowest order in the small parameter $k_R d$, where $1/k_R$ is the characteristic length scale over which the resonator mode varies appreciably and d is the characteristic dimension of the contact area S from which the resonator is suspended. For typical structures that exhibit high- Q mechanical resonances, $k_R d \ll 1$ is comfortably satisfied. This justifies the weak coupling approximation and leads to a general expression for the associated dissipation $1/Q$ in terms of the overlaps between the scattering modes and the resonator mode. In the limit $d \rightarrow 0$ the leading contribution is obtained by replacing the scattering modes by the free (unperturbed) modes of the supports, which yields²¹

$$\frac{1}{Q} = \frac{\pi}{2\rho_s\rho_R\omega_R^3} \int_q \left| \int_S d\bar{S} \cdot \left(\boldsymbol{\sigma}_q^{(0)} \cdot \bar{\mathbf{u}}'_R - \boldsymbol{\sigma}'_R \cdot \bar{\mathbf{u}}_q^{(0)} \right) \right|^2 \times \delta[\omega_R - \omega(q)]. \quad (1)$$

Here $\boldsymbol{\sigma}'_R$ and $\bar{\mathbf{u}}'_R$ are the stress and displacement fields associated with the normalized resonator mode, $\boldsymbol{\sigma}_q^{(0)}$ and $\bar{\mathbf{u}}_q^{(0)}$ are the analogous fields for the continuum of support modes labeled by q [eigenfrequencies $\omega(q)$], and ρ_s and ρ_R are, respectively, the densities of the substrate and resonator materials. The resonator mode should satisfy either (i) free or (ii) clamped boundary conditions at the contact area S depending on the behavior of the eigenmode when S is small, while the unperturbed support modes should satisfy the converse. These homogeneous boundary conditions correspond, respectively, to $d\bar{S} \cdot \boldsymbol{\sigma}'_R = 0$ and $\bar{\mathbf{u}}'_R = 0$ so that only one of the two terms in the surface integral is finite. Physical examples of case (i) are pedestal geometries, such as microspheres,

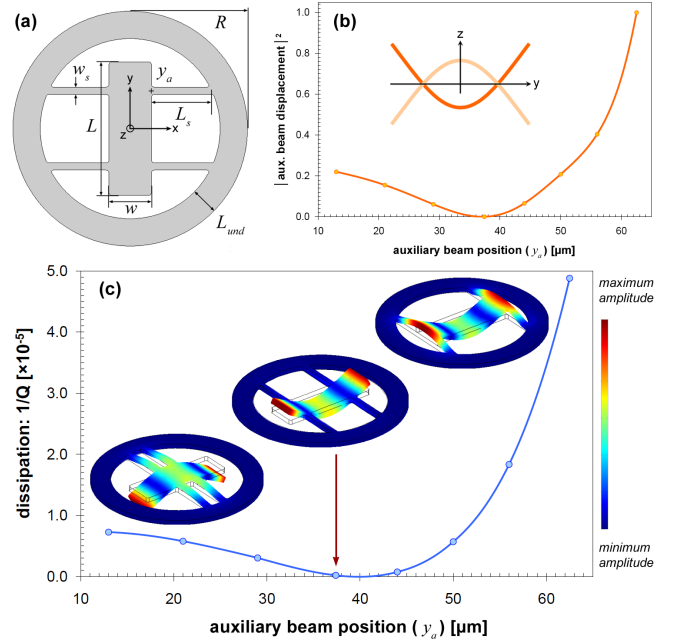


FIG. 1: Mapping out phonon-tunneling dissipation in a free-free resonator. (a) Schematic diagram of the resonator geometry. (b) Normalized squared center of mass displacement of a single auxiliary-beam-central-resonator contact calculated via FEM (the inset shows the profile of the free-free mode as approximated by Euler-Bernoulli theory). (c) Simulated dissipation [cf. Eq. 2] as a function of the auxiliary beam’s y -coordinate (y_a). Values corresponding to 8 discrete geometries were calculated here with $t = 6.67 \mu\text{m}$, $w_s = 7 \mu\text{m}$, $w = 42 \mu\text{m}$, $L = 132 \mu\text{m}$, $R = 116 \mu\text{m}$, and $L_{\text{und}} = 27 \mu\text{m}$ —the line is simply a guide for the eye. The FEM calculated mode shapes correspond to the three extreme examples of the resonator design, from left to right: auxiliary beams near the resonator center ($y_a = 13 \mu\text{m}$), beams near the ideal nodal position ($y_a = 37.4 \mu\text{m}$), and beams attached at the ends ($y_a = 62.5 \mu\text{m}$). The theoretical clamping loss limit $1/Q_{\text{th}}$ for nodal positioning is always finite with the geometry closest to this position (indicated by the arrow) yielding $1/Q_{\text{th}} \approx 2 \times 10^{-7}$.

microdisks, or microtoroids, when the pedestal has good impedance match with the substrate and is thus included in the support. On the other hand examples of case (ii) include the planar structures investigated here, where the supports consist of the portion of the structure that is not free-standing. Further details about the scope and validity of Eq. (1) are given in the SI Appendix A.

Though the aforementioned framework is completely general, in order to investigate the predictive power of our approach, we focus specifically on the flexural modes of a symmetric plate geometry of thickness t that is inscribed in a circle of radius R , with the contact area S corresponding to the outer rim of an idealized circular undercut (undercut distance of L_{und}). To calculate the theoretical Q -values of such devices via Eq. (1) we have developed a numerical solution technique that determines the resonator eigenmode and eigenfrequency

via FEM (with $\bar{u}'_R = 0$ at S) and uses a decomposition into cylindrical modes for the support, which is approximated by the substrate modelled as an isotropic elastic half-space. The latter approximation is expected to be quantitatively precise for the low-lying flexural resonances when the underetched gap between the suspended structure and the substrate satisfies $h < R$ (where h is the gap height), and the largest resonant wavelength for elastic wave propagation in the substrate is smaller than the relevant length scales characterizing the mounting of the sample (see below). The aforementioned weak coupling condition, $k_R d \ll 1$, follows in this case from $t \ll R$. From Eq. (1) we obtain [cf. SI Appendix A for details of this derivation]

$$\frac{1}{Q} = \frac{\pi}{2\rho_s \rho_R \omega_R} \sum_{n,\gamma} \frac{|f_{z,n}|^2}{c_\gamma^3} \tilde{u}_{n,\gamma}(\omega_R R/c_\gamma, \nu_s), \quad (2)$$

where we use cylindrical coordinates and introduce the dimensionless displacements $\tilde{u}_{n,\gamma}(\tilde{q}, \nu_s) = 2\pi \int_0^{\pi/2} d\theta \sin \theta |u_{\tilde{q},\gamma;z}^{(0)}(0, \nu_s)|^2 J_n^2(\tilde{q} \sin \theta)$ and the linear stress Fourier components $f_{z,n} = \int_S d\tilde{S} \cdot \boldsymbol{\sigma}'_R \cdot \hat{z} e^{in\phi}$ with $n = 0, \pm 1, \pm 2, \dots$. Here $\gamma = l, t, s$ labels the different types of relevant plane-wave modes $\bar{u}_{\tilde{q},\gamma;z}^{(0)}(\tilde{r}, \nu_s)$ of the half-space⁴⁴ [i.e. longitudinal (l), transverse SV (t), and surface acoustic waves (s) given that transverse SH waves do not contribute] with c_γ the corresponding speed of sound — as determined by the density ρ_s , Poisson ratio ν_s , and Young's modulus E_s of the substrate. We adopt spherical coordinates for the incident wave vector \tilde{q} with polar angle θ . It is straightforward to generalize the above to in-plane modes and to plate geometries inscribed in a rectangle. Furthermore, we stress that the rim need not be continuous, as in cases where the resonator volume contacts the support at a disjoint set of small areas.

For experimental verification of our solver, we have developed “free-free” micromechanical resonators consisting of a central plate (resonator) of length L and width w suspended by four auxiliary beams as depicted in Fig. 1(a). These structures are etched from a high-reflectivity monocrystalline distributed Bragg reflector (DBR) — as described in the Methods Section, suited for Fabry-Perot-based optomechanical systems⁴⁵. The devices used in this study constitute a variant of the previously demonstrated free-free flexural design in which auxiliary beams with widths $w_s \ll w$ and lengths $L_s = \lambda_t/4$ (where λ_t is the resonant wavelength for the propagation of torsional waves) placed at the nodes of the central resonator mode provide noise filters to suppress support-induced losses³. A major drawback with the $\lambda_t/4$ -beam design is that the resulting auxiliary beam length can be excessive. In fact for the eigenfrequencies investigated in this work, the corresponding beam length ($> 400\mu\text{m}$ at 1.7MHz) leads to a proliferation of low frequency flexural resonances that compromise the stability of the optical cavity and render mode identification difficult. We circumvent this issue by utilizing instead a reduced auxil-

iary beam length $L_s \ll \lambda_t/4$ chosen to avoid matching flexural resonances.

The free-free design provides an ideal platform to isolate and measure phonon tunneling dissipation: first, by altering the attachment position of the auxiliary beams, this design allows for a significant variation of geometry, while approximately preserving the frequencies and effective surface-to-volume ratios of the resonators. As these characteristics are kept constant, one can rule out the influence of additional damping mechanisms (specifically those driven by internal losses and surface effects) on the variation in Q and hence isolate support-induced losses in the measured devices. Second, the free-free resonators provide an intuitive illustration of the strong geometric character of support-induced dissipation. Intuitively, the clamping loss will be proportional to the elastic energy radiated through the auxiliary beams which should approximately scale as the squared deflection of their contacts with the central resonator [cf. Fig. 1 panels (b) and (c)]. Thus varying the contact position of the auxiliary beams results in a characteristic modulation of the damping rate which approximately maps out the central resonator mode shape. As expected, the minimum-loss design corresponds to the geometry in which the auxiliary beams are attached at the nodes of the fundamental resonance of the central resonator. It is interesting to note that the theoretical clamping loss limit $1/Q_{\text{th}}$ for nodal positioning is always *finite* as described in [Fig. 1(c)].

For mode identification we compare the optically measured resonator frequencies (as a function of the auxiliary beam position) with the theoretical eigenfrequency response. The simulated values are generated using the geometric parameters determined via careful analysis of the completed resonators (cf. SI Appendix B). As can be seen in Fig. 2(b), in addition to the symmetric free-free resonance, there is also an antisymmetric eigenmode with comparable frequency. We observe no mode-coupling between these resonances, which is consistent with the specific mirror symmetries of the structure. The frequencies are accurately reproduced by the FEM simulation if we allow for frequency offsets that are solely dependent on the mode parity (262 kHz offset for the free-free mode and 89 kHz offset for the anti-symmetric mode). We attribute these shifts to a materials-related dissipation mechanism, involving both surface and bulk contributions (see SI Appendix C for further details).

All dissipation measurements have been performed at high vacuum ($\approx 10^{-7}$ mbar) and at cryogenic temperatures (20 K) in order to suppress fluidic and thermoelastic damping in the devices. Under these conditions, we record quality factors spanning 1.4×10^4 to 5.1×10^4 (cf. Fig. 3), with the minimum Q corresponding to the free-free mode of devices with an auxiliary position of $62.5\mu\text{m}$ and $R = 116\mu\text{m}$, and with the maximum Q to the geometry closest to nodal positioning ($37.4\mu\text{m}$) for the same radius and type of mode. For the symmetric mode, we readily observe the expected characteristic modulation in Q as a function of the placement of

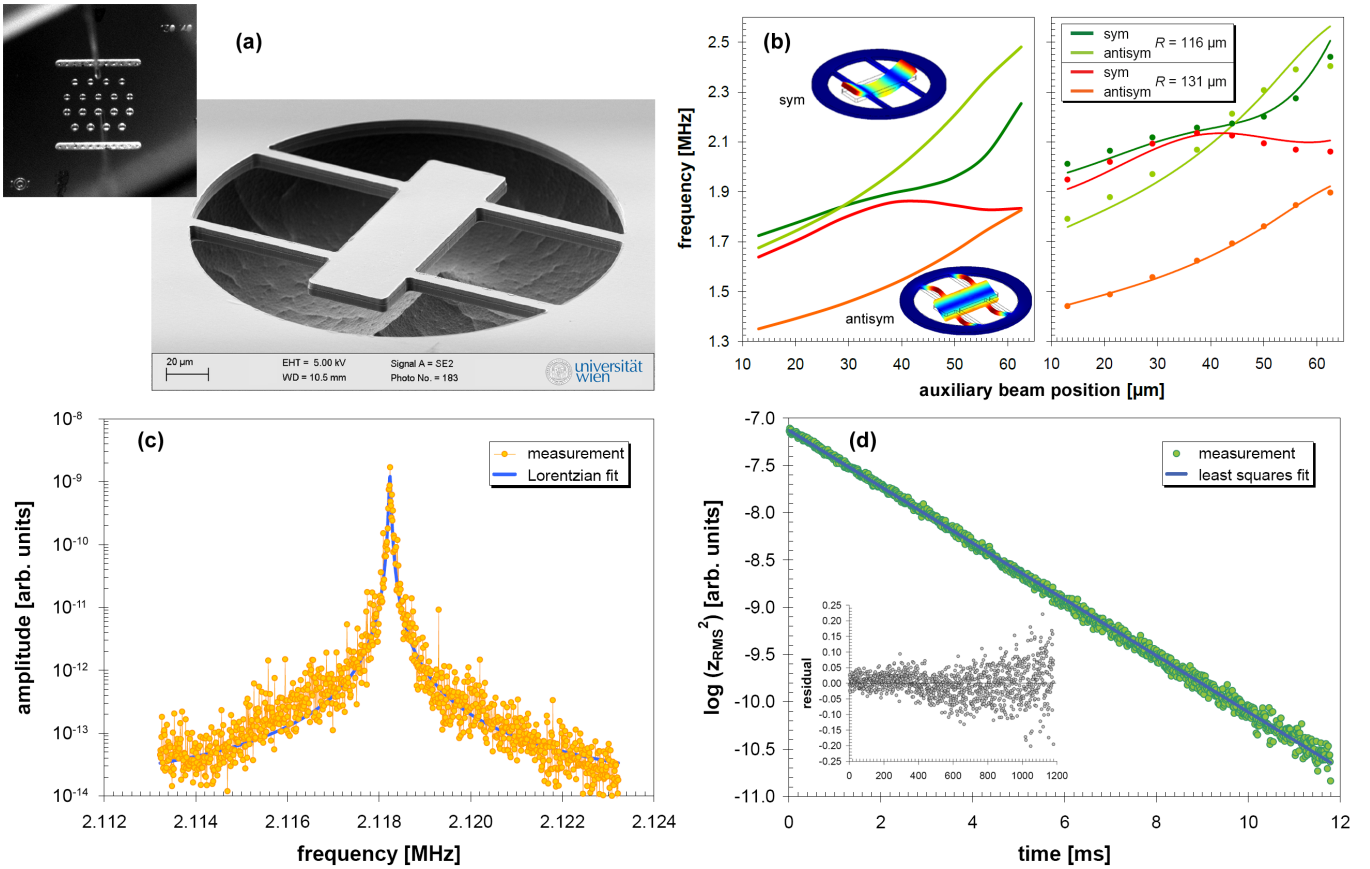


FIG. 2: Characterization of the completed free-free resonators. (a) Optical micrograph of the 5 mm×5 mm chip containing the batch-fabricated microresonators as well as an electron micrograph highlighting a single suspended structure. (b) Simulated (left) and measured (right) eigenfrequencies as a function of the auxiliary beam y -coordinate. The measured values (discrete points) show excellent agreement with the simulated dataset, albeit with a slight offset dependent on the parity of the mode. The fitting lines in the right plot correspond to a mean frequency offset of 262 kHz for the symmetric free-free modes and 89 kHz for the neighboring antisymmetric modes (inset shows the FEM derived mode shape of the antisymmetric resonance). Lower panel — examples of the fitting techniques utilized for Q -value extraction including: (c) Lorentzian fitting of the free-free resonance (captured on a spectrum analyzer) for a device with $R = 116 \mu\text{m}$ and $y_a = 29 \mu\text{m}$ resulting in $Q = 4.5 \times 10^4$; and (d) ringdown fitting of the same device using linear regression of the natural log of the mean-square of the free-ringdown signal captured single-shot with a high speed oscilloscope yielding $Q = 4.46 \times 10^4$. The inset includes the residuals to the linear fit showing an excellent agreement with the expected exponential decay.

the auxiliary beams (cf. Fig. 1) with a relative variation of $\Delta Q_{\text{exp}}/Q_{\text{exp}} \sim 260\%$ ($\sim 80\%$) for $R = 116 \mu\text{m}$ ($R = 131 \mu\text{m}$). At the same time, the frequency variation is kept small “qua design”, with a range of $\Delta f/f \sim 20\%$ ($\sim 10\%$). In contrast the Q -values for the antisymmetric mode are nearly constant with $Q \approx 2.1 \times 10^4$ [Fig. 3(c)]. This is expected as the theoretical support-induced loss for this mode is negligible. Additionally, as this resonance involves mainly deformations of the auxiliary beams, its dissipation is not expected to be correlated with the mode shapes of the central resonator. The damping of this mode is instead dominated by other sources of dissipation, most likely by the materials-related losses that are also responsible for the frequency shifts. Thus we obtain an independent corroboration that the characteristic Q -variation observed for the free-free mode is indeed induced by the modification of the geom-

etry rather than by the small frequency variation present in the devices.

In order to quantitatively compare the measurements with our numerical predictions, two additional issues must be considered: (i) our model only captures support-induced losses, while other loss mechanisms may still contribute to the overall damping in the devices, and (ii) the parameters for the half-space model of the substrate must be properly chosen. Consideration (i), together with the fact that we have designed sets of resonators for which the frequencies and effective surface-to-volume ratios are kept approximately constant, implies that any additional damping mechanism that is relevant at low temperatures and high vacuum, but is insensitive to the variation in geometry, should contribute a constant offset $1/Q_*$ in the measured dissipation $1/Q_{\text{tot}}$. Consideration (ii) is non-trivial given the long-wavelength nature of the elas-

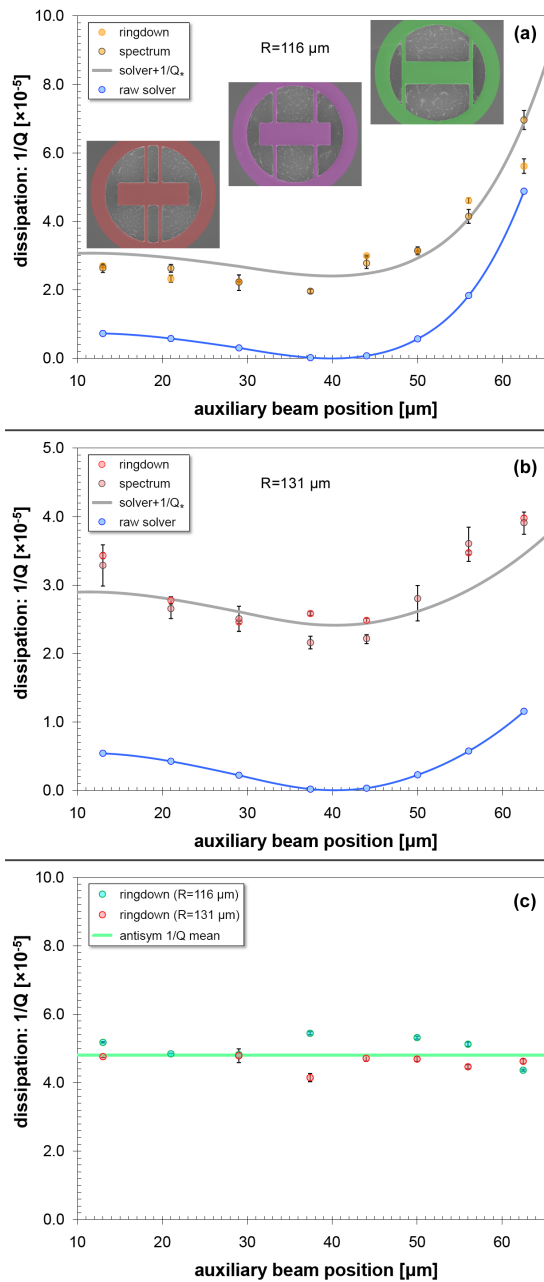


FIG. 3: Compiled dissipation results displaying excellent agreement between theory and experiment. (a) and (b) Comparison of experimental measurements at $T = 20$ K with theoretical dissipation values for the free-free mode of resonators with measured central dimensions of $132 \mu\text{m} \times 42 \mu\text{m}$ and radius $R = 116 \mu\text{m}$ and $R = 131 \mu\text{m}$, respectively. Both ringdown and spectrally-derived data are included, with values averaged over two nominally-identical chips. We include both raw simulated data as well as fitted data (continuous lines are a guide to the eye) incorporating a constant offset $1/Q_* = 2.41 \times 10^{-5}$. For the effective substrate we utilize the mechanical properties of Ti, which is the main constituent of the positioning system on which the chips are mounted ($\rho = 4540 \text{ kg/m}^3$, $E_s = 116 \text{ GPa}$, and $\nu_s = 0.34$). (c) Measured dissipation for the antisymmetric mode of the same structures exhibiting a lack of geometric dependence.

tic waves radiated into the substrate. For an average resonator frequency $\approx 2.12 \text{ MHz}$ estimates of the maximum wavelength for the freely-propagating elastic waves yield a value of $\approx 2.5 \text{ mm}$, which largely exceeds the wafer thickness ($300 \pm 25 \mu\text{m}$). Thus, the mechanical materials parameters for the substrate should be determined by the properties of the underlying stage and positioning mechanism in the cryostat rather than by those of the chip itself. Hence, we assume for the half-space the mechanical properties of polycrystalline commercially-pure (grade 2) titanium (cf. Fig. 3), of which the bulk of the structure beneath the resonator consists. Taking all of this into account, the theory shows remarkable agreement with the measured dissipation (as shown in Fig. 3). It is important to note that the only free parameter used in the model of the free-free mode is a constant offset of $1/Q_* = 2.41 \times 10^{-5}$. Although the exact nature of the corresponding dissipation mechanism is currently unknown, we assume that it arises from materials losses in the resonator epi-structure. As our design isolates the support induced-losses, these results establish the first systematic test of phonon tunneling dissipation in mechanical resonators.

It should be noted that most commercially viable resonators operate in a regime where TED dominates, and in some instances intuitive understandings of the support-induced damping^{3,5,36} have allowed for its suppression below other limiting damping mechanisms. Nonetheless, if current efforts to minimize TED in such structures at room temperature are successful²⁵, support-induced losses may pose the next challenge for maximizing Q . On the other hand, in fundamental research thrusts employing high vacuum and cryogenic systems, support-induced losses can become a dominant factor^{37,38}. For example, the free-free designs explored here provide a route to minimize support-induced losses for application in optomechanical experiments utilizing the micromechanical resonator as an end mirror in a high-finesse Fabry-Perot cavity⁴⁵. To gauge the relevance of our “free-free” micromirror design in this context, it is instructive to compare the fundamental limit at nodal positioning $Q_{\text{th}} \approx 5 \times 10^6$ and the maximum Q -value measured of 5.1×10^4 , with the corresponding results for the fundamental flexural mode of a clamped bridge of comparable dimensions. In fact for the typical dimensions considered, as required for integration in a high-performance Fabry-Perot cavity, we obtain a theoretical limit $Q_{c-c} \sim 10^3$ in line with prior measurements on monocrystalline DBR optomechanical structures⁴⁶.

Given the scale independent nature of support-induced losses, our solver applies equally well to nanoscale mechanical devices. We find that for a recent demonstration of a nanomechanical doubly-clamped beam coupled to a superconducting qubit at mK temperatures⁴⁷, the measured values for the resonator’s maximum Q ($\approx 6 \times 10^4$) can be understood solely via the phonon-tunneling loss model (beam geometry of $0.3 \mu\text{m} \times 0.18 \mu\text{m} \times 6 \mu\text{m}$) which predicts a Q of 5.4×10^4 , in excellent agreement with the

experimental value.

In conclusion, we have developed an efficient FEM-enabled numerical method for predicting the support-induced dissipation in micro- and nanoscale mechanical resonators. In combination with existing models for other relevant damping channels (e.g. fluidic and TED^{24,25}), our “phonon-tunneling” solver makes further strides towards accurate prediction of the mechanical quality Q . Furthermore, we demonstrate a stringent experimental test of the corresponding theory using resonators engineered to isolate support-induced losses. Our results demonstrate unambiguously that phonon-tunneling plays a significant role in the mechanical dissipation of these devices and illustrates the strong geometric character of this fundamental damping mechanism. Finally, we note that the weak coupling approximation underlying our treatment is more general than the condition of small contact area. Thus, our numerical solver can in principle be extended to other relevant scenarios such as systems in which the stresses at the contact are strongly suppressed, as for example phononic-band-gap structures³⁸.

GDC is a recipient of a Marie Curie Fellowship of the European Commission (EC). Additional financial support is provided by the EC (projects MINOS, IQOS), the Austrian Science Fund (projects START, L426, SFB FoQuS), and the European Research Council (ERC StG QOM). Microfabrication was carried out at the Zentrum für Mikro- und Nanostrukturen (ZMNS) of the Technische Universität Wien. GDC gratefully acknowledges Stephan Puchegger and Markus Schinnerl for assistance with scanning electron microscopy and focused ion beam milling. IWR acknowledges financial support via the Nanosystems Initiative Munich, KW via the Austrian Research Promotion Agency (FFG).

I. METHODS

Epitaxial Materials Structure and Resonator Fabrication Procedure – The materials structure for our high reflectivity resonators consists of 40.5-periods of alternating quarter-wave GaAs (high index) and AlAs (low index) layers grown lattice-matched to an off-cut monocrystalline germanium substrate. The ideal total thickness of the heterostructure is 6857.6 nm, with individual layer thicknesses of 77.6 nm and 91.9 nm for the GaAs and AlAs respectively; yielding a nominal peak reflectivity at 1064 nm, as with our previous optomechanics experiments⁴⁶. With this design, the germanium substrate enables the use of a high-selectivity gas-phase etching procedure, based on the noble-gas halide XeF₂, in order to rapidly and selectively undercut the underlying germanium substrate. Thus we realize a free-standing epitaxial Bragg mirror via a simple and fast-turnaround fabrication procedure. The details of both the epitaxial materials design and microfabrication procedure are covered in Ref. 48.

Measurement technique – To characterize the fre-

quency response of our microresonators we utilize a custom-built optical fiber interferometer featuring a continuous flow ⁴He cryostat as the sample chamber⁴⁹. High sensitivity displacement resolution is achieved in this system via optical homodyne interferometry. Cryogenic testing of these devices is necessitated due to the limitations imposed by TED at room temperature. Estimations of the magnitude of TED is possible using the analytical and finite element models developed previously^{23–25}, which predict a Q -value of ~ 4000 for the current DBR composition and thickness at 1.8 MHz and 300 K — consistent with performed measurements. In order to avoid TED our cryostat enables interrogation down to 20 K (resulting in an estimated TED limited Q of 9.9×10^8); the minimum temperature is currently limited by the large view-port above the sample stage. Additionally, this system is capable of vacuum levels down to 2.5×10^{-7} millibar at cryogenic temperatures, removing any additional damping induced by fluidic, or squeeze film effects^{26–28}. The eigenmodes of the resonator are excited by driving a high-frequency (10 MHz) piezo disc soldered to a copper stage in thermal contact with the cold finger. For spectral characterization, the piezo disc is driven with white noise and the resonator frequency response is recorded on a low-noise spectrum analyzer. For the free-ringdown measurements, the decay of a resonantly excited device is recorded in a single shot on a high-speed oscilloscope.

II. SUPPLEMENTARY INFORMATION

Appendix A: Numerical calculation of Q -values

A rigorous derivation of Eq. (1) is given in Ref. 21. Alternatively, if one uses a decomposition of the displacement field in terms of the unperturbed support modes and the discrete modes of the resonator volume, Eq. (1) follows simply from applying Fermi’s Golden rule to phonon decay with the interaction Hamiltonian between the resonator volume (labeled \langle) and the surrounding supports (labeled \rangle) given by $\int_S d\vec{S} \cdot \boldsymbol{\sigma}_\rangle \cdot \vec{u}_\langle$ for case (i) and $-\int_S d\vec{S} \cdot \boldsymbol{\sigma}_\langle \cdot \vec{u}_\rangle$ for case (ii). Within this framework, it is straightforward to realize that the validity of Eq. (1) is more general than the condition $k_R d \ll 1$ and will also apply to systems in which the stresses at the contact are exponentially suppressed, like for example phononic-band-gap structures. In general the decomposition between “resonator volume” and “supports” consistent with the weak coupling condition need not be unique. For our case the use of this master formula is completely equivalent to prior intuitive approaches based on forcing the substrate with the stress source generated by the resonator, as can be shown rigorously by using —for the elastic Green’s function of the substrate —a spectral decomposition in terms of its free modes. Finally, one should note that Eq. (1) assumes that the resonance is spectrally resolved and that the support-induced

frequency shifts are small compared with the free spectral range²¹. Thus, in the presence of mode-coupling^{37,42} our treatment remains valid provided that the mode-coupling is not dominated by support-induced interactions, which includes the case where it is accounted for by FEM assuming perfect clamping and excludes cases where symmetry-breaking induced by the support is relevant. In the particular case studied here, the suspended structure has reflection symmetries with respect to the $x - y$, $x - z$, and $y - z$ planes; while the entire structure including the substrate is only invariant under the latter two, allowing one to classify the modes accordingly.

To derive Eq. (2) from Eq. (1) we adopt for the free elastic half-space, modelling the decoupled support, a decomposition into eigenmodes $\bar{u}_{q,\theta,n,\gamma}^{(0)}(\bar{r})$ (with $n = 0, \pm 1, \pm 2, \dots$ and $q > 0$) that have axial symmetry with respect to z (cf. Fig. 1). These are related to the plane wave eigenmodes $\bar{u}_{\bar{q},\gamma}^{(0)}(\bar{r})$ by

$$\bar{u}_{q,\theta,n,\gamma}^{(0)}(\bar{r}) = \frac{1}{\sqrt{2\pi}} \int_{-\pi}^{\pi} d\varphi (-i)^n e^{in\varphi} \bar{u}_{\bar{q}(q,\theta,\varphi),\gamma}^{(0)}(\bar{r}) \quad (\text{A1})$$

where $\gamma = l, t, s$ labels the different types of relevant modes [i.e. longitudinal (l), transverse SV (t), and SAW (s) given that SH waves do not contribute] and we adopt spherical coordinates for the incident wavevector $\bar{q}(q, \theta, \varphi) = q(\sin \theta \cos \varphi, \sin \theta \sin \varphi, \cos \theta)$ [$\theta = \pi/2$ for $\gamma = s$ and $\theta \leq \pi/2$ otherwise]. We note that for the suspended plate geometry considered, the appropriate resonator mode satisfies $\bar{u}'_R = 0$ at the contact S so that we need to evaluate the second term in Eq. (1).

The thin plate condition $t \ll R$ directly allows us, given the flexural nature of the modes of interest, to neglect stresses at S that are parallel to the substrate with the possible exception of bending-moment

contributions⁴⁴ — this also applies if there are small transverse dimensions comparable to t . However the bending-moment contributions also become negligible in the limit $t/R \rightarrow 0$ as can be shown by using: (i) that given $\omega_R \ll c_\gamma/R \forall \gamma$, we can Taylor expand $\bar{u}_{q,\theta,n,\gamma}^{(0)}(\bar{r})$ at the origin in the integral over S , (ii) that we can assume relevant stresses to be concentrated around the ends of the auxiliary beams so that the bending moments at S are mostly oriented along y , (iii) the reflection symmetries, and (iv) that, barring interference effects, these bending-moment contributions are at most of relative order²¹ $k_R t$ — here $k_R = (12\rho_R/E_R)^{1/4} \sqrt{\omega_R/t}$ is the resonant wavevector for the propagation of flexural waves. Thus, we find that for all mode types other than $-+$ [antisymmetric (symmetric) with respect to R_x (R_y)] the correction associated to neglecting the bending moments scales as $\Delta Q/Q \sim (k_R t)^2$, while for $-+$ modes it scales as $\Delta Q/Q \sim k_R t$ (note that $L \sim R$). In turn, we find that the relative error in using Eq. (1), arising from the weak coupling approximation, scales in this case as $\Delta Q/Q \sim |\Delta\omega_R|/\omega_R \sim |\Delta_I(\omega_R)|/\omega_R \sim (k_R t)^3$, where the phonon-tunneling induced frequency shift is approximated by $\Delta_I(\omega_R) \approx -(2/\pi) \int_0^\infty d\omega I(\omega)/\omega$ with $I(\omega)$ the environmental spectrum²¹.

Hence we can assume $d\bar{S} \cdot \sigma'_R \parallel \hat{z}$ and neglect the variation of $\bar{u}_{q,\theta,n,\gamma}^{(0)}(\bar{r})$ across the thickness t (i.e. the z -dependence at S), so that the support modes only enter into Eq. (1) through $u_{q,\theta,n,\gamma;z}^{(0)}(\bar{r})|_{z=0}$. To determine the latter we adopt cylindrical coordinates $\bar{r} = (r \cos \phi, r \sin \phi, z)$, substitute into Eq. (A1) the plane wave expressions for $u_{\bar{q}(q,\theta,\varphi),\gamma;z}^{(0)}(\bar{r})$, exploit that reflection at the free surface preserves the tangential component of the wavevector, and use the Bessel integral $J_n(x) = \frac{1}{2\pi} \int_{-\pi}^{\pi} e^{-i(n\phi - x \sin \phi)} d\phi$. Thus we obtain

$$u_{q,\theta,n,\gamma;z}^{(0)}(\bar{r})|_{z=0} = \frac{(-i)^n}{\sqrt{2\pi}} u_{\bar{q}(q,\theta,\varphi),\gamma;z}^{(0)}(0) \int_{-\pi}^{\pi} e^{-i[n\varphi + r q \sin \theta \cos(\phi - \varphi)]} d\varphi = \sqrt{2\pi} u_{\bar{q}(q,\theta,\varphi),\gamma;z}^{(0)}(0) J_n(r q \sin \theta) e^{in\phi}, \quad (\text{A2})$$

that substituted into $\hat{z} \cdot \bar{u}_{\bar{q}}^{(0)}(\bar{r})$ in Eq. (1) leads to Eq. (2) after using $\int_{\bar{q}} \rightarrow \sum_{n,\gamma} \int_0^\infty dq q^{d_\gamma-1} \int_0^{\pi/2} d\theta (\pi/2)^{d_\gamma-3} (\sin \theta)^{d_\gamma-2} \theta$ (d_γ is the dimensionality, i.e. $d_\gamma = 2$ for $\gamma = s$ and $d_\gamma = 3$ for $\gamma \neq s$), performing the substitution $\omega = c_\gamma q$ (for each γ), and integrating over ω . Subsequently, substitution of the explicit expressions for the plane wave eigenmodes $\bar{u}_{\bar{q},\gamma}^{(0)}(\bar{r})$ (see for example Appendix A in Ref. 21) and $v = \cos \theta$ into the definition of $\tilde{u}_{n,\gamma}(\tilde{q}, \nu_s)$ allows us to obtain:

$$\tilde{u}_{n,l}(\tilde{q}, \nu_s) = \frac{1}{\pi^2} \int_0^1 dv \frac{(1 - 2\alpha + 2\alpha v^2)^2 v^2 J_n^2(\tilde{q} \sqrt{1 - v^2})}{[4\alpha^{3/2} \sqrt{1 - \alpha} + \alpha v^2 (1 - v^2) v + (1 - 2\alpha + 2\alpha v^2)^2]^2} \Big|_{\alpha=\alpha[\nu_s]}$$

$$\tilde{u}_{n,t}(\tilde{q}, \nu_s) = \frac{4}{\pi^2} \left\{ \int_0^{\sqrt{1-\alpha}} dv \frac{(1 - \alpha - v^2)(1 - v^2) v^2 J_n^2(\tilde{q} \sqrt{1 - v^2})}{16(1 - \alpha - v^2)(1 - v^2) v^2 + (2v^2 - 1)^4} \right.$$

$$\begin{aligned} & + \int_{\sqrt{1-\alpha}}^1 dv \frac{(\alpha-1+v^2)(1-v^2)v^2 J_n^2(\tilde{q}\sqrt{1-v^2})}{[4\sqrt{\alpha-1+v^2}(1-v^2)v+(2v^2-1)^2]^2} \Bigg|_{\alpha=\alpha[\nu_s]} \\ \tilde{u}_{n,s}(\tilde{q}, \nu_s) = & \frac{C^2(\alpha)}{\pi} \left[\sqrt{1-\alpha\xi^2(\alpha)} - \frac{1-\xi^2(\alpha)/2}{\sqrt{1-\xi^2(\alpha)}} \right]^2 J_n^2(\tilde{q}) \Bigg|_{\alpha=\alpha[\nu_s]} \end{aligned} \quad (\text{A3})$$

where we use the ratio $\alpha \equiv (c_t/c_l)^2 = (1-2\nu_s)/2(1-\nu_s)$ for the supports' material (ν_s is the corresponding Poisson ratio). In turn $\xi(\alpha)$ is the ratio of the propagation velocity of surface waves to c_t , which is a function of α that is always less than unity⁴⁴, and

$$\begin{aligned} C(\alpha) = & \left\{ \frac{2-\xi^2(\alpha)}{[1-\xi^2(\alpha)]^{3/2}} [\xi^4(\alpha)/4 + \xi^2(\alpha) - 1] \right. \\ & \left. + \frac{2-\alpha\xi^2(\alpha)}{\sqrt{1-\alpha\xi^2(\alpha)}} \right\}^{-1/2}. \end{aligned} \quad (\text{A4})$$

The sum in Eq. (2) can be reduced to a sum over $n \geq 0$

by noting that $J_{-n}(x) = (-1)^n J_n(x)$ and that as the resonator mode is real, the linear stress Fourier components satisfy $f_{z,-n} = f_{z,n}^*$. Furthermore, the length of the central resonator L is comparable to the radius R and we focus on low-lying resonances of the suspended structure so that the aforementioned condition $\omega_R \ll c_\gamma/R \forall \gamma$ is always satisfied. This implies $|\sum_\gamma \tilde{u}_{m,\gamma} / \sum_\gamma \tilde{u}_{n,\gamma}| \ll 1$ for $m > n$ and $\sum_\gamma \tilde{u}_{n,\gamma} \neq 0$, which can be understood by considering the behavior of the Bessel functions for small arguments. Thus we find that in Eq. (2) the sum over the index n is dominated by the first non-vanishing term as determined by the reflection symmetries R_x, R_y . The latter also imply ($n = 0, 1, 2, \dots$):

$$\begin{aligned} f_{z,2n}^{++} &= R \int_{-\pi}^{\pi} d\phi \int_{-\frac{t}{2}}^{\frac{t}{2}} dz \hat{r} \cdot \boldsymbol{\sigma}_R^{++}(\bar{r}) \cdot \hat{z} \cos 2n\phi, \\ f_{z,2n+1}^{+-} &= R \int_{-\pi}^{\pi} d\phi \int_{-\frac{t}{2}}^{\frac{t}{2}} dz \hat{r} \cdot \boldsymbol{\sigma}_R^{+-}(\bar{r}) \cdot \hat{z} \sin(2n+1)\phi, \\ f_{z,2n+1}^{-+} &= R \int_{-\pi}^{\pi} d\phi \int_{-\frac{t}{2}}^{\frac{t}{2}} dz \hat{r} \cdot \boldsymbol{\sigma}_R^{-+}(\bar{r}) \cdot \hat{z} \cos(2n+1)\phi, \\ f_{z,2n}^{--} &= R \int_{-\pi}^{\pi} d\phi \int_{-\frac{t}{2}}^{\frac{t}{2}} dz \hat{r} \cdot \boldsymbol{\sigma}_R^{--}(\bar{r}) \cdot \hat{z} \sin 2n\phi, \\ f_{z,2n+1}^{++} &= f_{z,2n}^{+-} = f_{z,2n}^{-+} = f_{z,2n+1}^{--} = 0; \end{aligned} \quad (\text{A5})$$

where the resonator mode of type α, β satisfies $R_x \boldsymbol{\sigma}_R^{\alpha,\beta} = \alpha \boldsymbol{\sigma}_R^{\alpha,\beta}$ and $R_y \boldsymbol{\sigma}_R^{\alpha,\beta} = \beta \boldsymbol{\sigma}_R^{\alpha,\beta}$. To efficiently extract the above from the FEM simulation we convert them into volume integrals using an adequate Gaussian weight so that for example, for a fully symmetric mode we have

$$f_{z,2n}^{++} = \lim_{a_* \rightarrow 0} \frac{2}{\sqrt{\pi} a_*} \int_V d\mathbf{r}^3 e^{-\left(\frac{r-R}{a_*}\right)^2} \hat{r} \cdot \boldsymbol{\sigma}'_R(\bar{r}) \cdot \hat{z} \cos 2n\phi, \quad (\text{A6})$$

where we again use cylindrical coordinates and V denotes the resonator volume. In addition we exploit that the reflection symmetries naturally allow to perform the FEM simulation on a single quadrant. Thus, numerical evaluation can be conveniently performed using a fixed a_* and a mesh size M such that $(V/4M)^{1/3} < a_* \ll t$. We have checked the convergence and estimate the numerical error to be of order 5%.

Numerical simulations of the resonator mode are

performed with the aid of COMSOL multiphysics. Accurate three-dimensional CAD models representing the resonator geometry are generated using Solidworks (matched with high quality SEM images as described in Appendix B) and the bidirectional interface between the two programs is exploited in order to perform a parametric sweep of the auxiliary beam contact position for determining the pertinent information about the relevant mode; namely, its eigenfrequency, linear stress Fourier

components $f_{z,n}$, and normalization constant. In this instance a single CAD file is used with a global variable incorporated in order to control the lateral position of the auxiliary beams with respect to the center of the central resonator. We use for the mechanical properties of our single-crystal resonators an anisotropic materials model incorporating the elastic stiffness matrix for the epitaxial structure as obtained from a weighted average between the relative content of GaAs and AlAs (46.37% GaAs / 53.63% AlAs). The corresponding parameters are: $C_{11} = 119.6$ GPa, $C_{12} = 55.5$ GPa, $C_{44} = 59.1$ GPa, and $\rho_R = 4483$ kg/m³. The resonator axes are aligned along $\langle 100 \rangle$ (zinc-blende structure). Note that we ignore the 6-degree misorientation of the germanium substrate as we have checked that it has a negligible impact (error of 0.3%) on the simulated frequency response of the resonators.

We note that our generic symmetric inscribed structure includes the particular case of bridge geometries with no undercut for which a simple variant of the method used in Ref. 21 allows us to obtain an analytical approximation for the Q -value of the fundamental mode Q_{c-c} valid for $3\pi t/2L \ll 1$. Our scenario differs from the one considered in Ref. 21 in two ways: (i) there is now a single half-space support instead of two and (ii) its free surface is oriented parallel to the beam's axis instead of perpendicular to it. Thus, for the fundamental flexural mode as the resonant wavelength in the support is much larger than the bridge length L , to lowest order in $(t/L)^2$ the stresses at both clamping points add coherently so that the overall effect of (i) is to double the dissipation. In turn (ii) implies that the roles of the dimensionless displacements for compression and bending are interchanged so that the dissipation of the vertical bending modes are further corrected by a factor of \tilde{u}_c/\tilde{u}_v . Thus if we consider that the support and resonator are made of the same material characterized by a Poisson ratio $\nu = 1/3$ we obtain

$$Q_{c-c} = \frac{0.92 L^5}{\pi^4 \nu t^4}. \quad (\text{A7})$$

Hence as a non-trivial check we have applied our numerical method to the fundamental mode of clamped-clamped square beam monolithic geometries with no undercut, $\nu = 1/3$, and aspect ratios L/t ranging from 15 to 40 and compared the results with those corresponding to Eq. (A7). We find a discrepancy ϵ that decreases monotonously from 20% to 4% which is consistent with the rough heuristic estimate $\epsilon \sim 3\pi t/2L$.

Appendix B: Analysis of Completed Devices

The resonator layout we have designed features 16 devices on chip, each with identical central resonator dimensions (nominally $130 \times 40 \mu\text{m}^2$). The 16 devices are divided into two sub-units featuring different outer radii (116 μm and 131 μm respectively), which are included in order to probe the effects of the auxiliary beam length on

the dissipation. Finally, each of the two subsets contains 8 variations of the auxiliary beam contact position, varying from the center to the extreme outer edge of the central beam, with a single design chosen to match the theoretically calculated node position (auxiliary beam positions of 13, 21, 29, 37.4, 44, 50, 56, and finally, $62.5 \mu\text{m}$). To ensure a thorough investigation of each geometry, two separate but nominally identical chips are measured.

Central to this study is an accurate determination of the geometric properties of the optomechanical resonators. Thus, we employ a variety of analytical techniques for the characterization of these devices as detailed below. We find that the actual thickness of the DBR is $6.67 \mu\text{m}$, the central resonator dimensions are enlarged by $1 \mu\text{m}$ at each free edge as compared with the nominal design values, and finally, L_{und} is destructively measured post characterization and found to be on average $27 \mu\text{m}$. In turn the microfabrication procedure detailed Ref. 48 entails $h \sim L_{\text{und}}$.

Thickness: In order to accurately determine the physical thickness of the resonators, we rely on measurements of the DBR reflectance spectrum. This procedure begins by recording the reflectance of the mirror stack (on wafer) as a function of wavelength via spectrophotometry. A transmission matrix model is then used to fit the measured high-reflectivity stop-band; the individual layer thicknesses are adjusted assuming constant (fixed percentage) growth errors for the constituent films. Note that the wavelength of peak reflectivity of the mirror is highly sensitive to variations in layer thickness. In fact for this structure, a 1 nm variation in the individual layer thickness shifts the wavelength of peak reflectivity by approximately 10 nm. Relying on accurate knowledge of the room temperature refractive index of the binary films, we realize a minimum wavelength resolution of ± 1 nm; thus, the thickness accuracy is better than 20 nm for the DBR. From this analysis we have determined that the actual thickness of the DBR is slightly shorter than desired at $6.67 \mu\text{m}$ with a peak on-wafer reflectance near 1060 nm at room temperature (ideal target thickness of $6.86 \mu\text{m}$, corresponding to a peak wavelength of 1078 nm at 300 K). The thickness is further verified by scanning probe measurement of the DBR following the anisotropic etch of the epitaxial layers. The profilometer provides an upper limit to the DBR thickness, as additional etching arising from surface sputtering of the Ge substrate is unavoidable. These measurements yield a conservative thickness estimate between $6.7 \mu\text{m}$ and $6.8 \mu\text{m}$, verifying the more accurate spectrophotometer derived value.

Resonator Dimensions: The lateral dimensions of the resonators are determined by obtaining high resolution micrographs of each individual structure in a field emission scanning electron microscope (Zeiss Gemini). Image analysis shows that the lateral dimensions of the resonators have expanded by $+1 \mu\text{m}$ on each edge, with the following results: reducing the nominal external support diameter by $2 \mu\text{m}$, increasing the auxiliary beam width from $5 \mu\text{m}$ to $7 \mu\text{m}$, and increasing the overall

lateral dimensions of the resonator by $2\ \mu\text{m}$ to $132\ \mu\text{m}$ and $42\ \mu\text{m}$. Additionally, a combination of process non-idealities (non-optimized exposure or development times) during lithography result in the formation of a $3\text{-}\mu\text{m}$ -radius fillet of at each corner of the device. These results are fed back into the CAD model of the resonator in order to generate the true resonator geometry for simulation. An overlay of the simulated resonator geometry and micrographs obtained via scanning electron microscopy can be seen in Fig. 3(a). Note that the resonators used in this study were not subject to potentially damaging energetic processes beyond the required plasma etching, including both SEM and FIB (as described below), until all dissipation measurements had been completed.

Undercut: In order to perform measurements of the support undercut distance, a dual beam SEM/FIB (Zeiss Gemini) is utilized to mill a window through the DBR and expose the underlying germanium. Because the GaAs/AlAs heterostructure is opaque to visible light, it is not possible to simply view the undercut distance with an optical microscope. This method allows for an accurate determination of the lateral etch distance below the supports. Image analysis yields an average distance of $27\ \mu\text{m}$ for the structures. Note that multiple chips of identical geometry were released simultaneously in a single process run, in order to ensure repeatability in the resonator dimensions. Selected measurements across the chip verify that the undercut length is constant for the resonators studied here (measured values fall between 26.5 and $28.2\ \mu\text{m}$).

Appendix C: Q -value and frequency measurements

We utilize two options for driving and characterizing the resonance of interest: (i) by applying broadband white noise to the piezo disc for extraction of the mechanical frequency spectrum (simultaneously driving all modes within the system bandwidth), and (ii) by exciting a desired mode resonantly with a sinusoidal voltage input, abruptly shutting off the drive, and then recording the free-ringdown of the structure. In the first method, Q is extracted by measuring the width of the resonance of interest, while in the latter, the single-shot amplitude decay time of the ringing structure provides the damping rate of the resonator.

For data analysis, we employ a combination of spectral fitting with a Lorentzian function, with linear-regression-based fitting of a decaying exponential in the case of the ringdown data. The envelope of the raw ringdown signal is created by first squaring the dataset (in order to utilize both the positive and negative components of the decaying sinusoid) and then averaging over a 10-20 period window (it is important to note that a typical ringdown dataset contains more than 1.5×10^3 periods of oscillation). Finally, to linearize the data, we simply take the natural logarithm of the mean-squared amplitude. In contrast to the single-shot ringdown datasets, the spec-

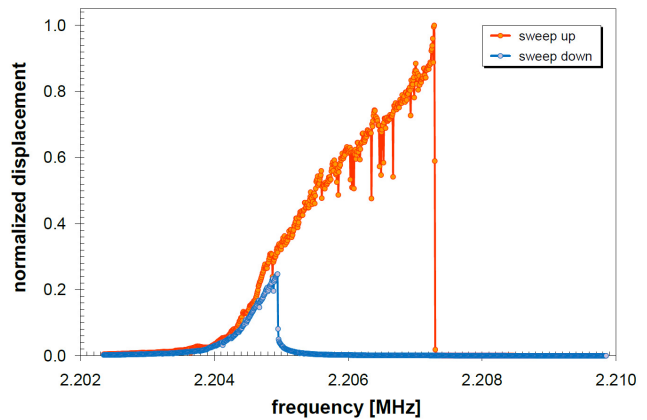


FIG. 4: Measured bistable response of the anti-symmetric mode.

tral measurements require multiple averages for a clean signal (typically $\sim 50 - 100$). The Lorentzian fit parameters include the amplitude, center frequency, and full width at half maximum (FWHM), with the latter two used for calculating Q from their ratio. The fast Fourier transform (FFT) of the ringdown signal can also be used to determine the eigenfrequency, while the $1/e$ decay time τ allows for the extraction of the resonator quality factor via the relation $\tau = Q/\pi f$.

Mode identification is realized by comparing the resonator frequency response as a function of geometry with the simulated eigenfrequency values. The modes are further distinguished by the relative geometric-induced non-linearity at resonance. The desired free-free mode remains linear to the limits of our piezoelectric-based inertial drive. On the other hand, the neighboring anti-symmetric mode exhibits a significant hardening spring Duffing response and can readily be driven into a bistable regime as shown in Fig. 4. Care is taken to drive this mode below the threshold for bistability to avoid complications in dissipation extraction. This marked difference in the responses of these two types of modes is consistent with their free-free versus clamped-clamped nature⁴.

To each dissipation mechanism there is an associated dispersive effect induced by the interactions with the corresponding environment that shifts the resonant frequencies. For a given resonance (ω_R) this shift can be positive or negative depending on whether the environmental spectrum is dominated, respectively, by modes with frequencies lower or higher than ω_R . In turn, the two types of modes have markedly different surface-to-volume ratios, larger for the antisymmetric resonance and smaller for the symmetric one; exhibit a positive shift which is substantially larger for the symmetric mode, and a “background” dissipation that is larger for the antisymmetric one (cf. Fig. 3). These facts can be reconciled by assuming that two materials-related dissipation mechanisms contribute to the “background”: a bulk one leading to an overall positive shift which is the same for both types of modes, and a surface one leading to a smaller negative

shift that naturally scales as the surface-to-volume ratio. In turn, theoretical estimates for the phonon-tunneling induced shift yield a negligible *negative* shift that should also follow the mode profile leading to a significant mod-

ulation that is not observed. Likewise mode coupling between the different resonators would also be incompatible with a constant shift.

-
- * These authors contributed equally to this work.
 † markus.aspelmeyer@univie.ac.at
- ¹ Craighead, H. G. Nanoelectromechanical systems. *Science* **290**, 1532 (2000).
 - ² Ekinci, K. L. & Roukes, M. L. Nanoelectromechanical systems. *Review of Scientific Instruments* **76**, 061101 (2005).
 - ³ Wang, K., Wong, A.-C. & Nguyen, C. T.-C. VHF free-free beam high-Q micromechanical resonators. *J. Microelectromech. Syst.* **9**, 347 (2000).
 - ⁴ Cleland, A. N. *Foundations of Nanomechanics* (Springer, Berlin, 2003).
 - ⁵ Clark, J., Hsu, W.-T., Abdelmoneum, M. & Nguyen, C.-C. High-Q UHF micromechanical radial-contour mode disk resonators. *J. Microelectromech. Syst.* **14**, 1298–1310 (2005).
 - ⁶ Lutz, M. *et al.* Mems oscillators for high volume commercial applications. In *Proc. Transducers, Solid-State Sensors, Actuators and Microsystems*. (2007). 14th Int. Conf.
 - ⁷ Sidles, J. A. *et al.* Magnetic resonance force microscopy. *Rev. Mod. Phys.* **67**, 249 (1995).
 - ⁸ Rugar, D., Budakian, R., Mamin, H. J. & Chui, B. W. Single spin detection by magnetic resonance force microscopy. *Nature* **430**, 329–332 (2004).
 - ⁹ Degen, C. L., Poggio, M., Mamin, H. J., Rettner, C. T. & Rugar, D. Nanoscale magnetic resonance imaging. *Proc. Natl Acad. Sci. USA* **106**, 1313–1317 (2009).
 - ¹⁰ Li, M., Tang, H. X. & Roukes, M. L. Ultra-sensitive nems-based cantilevers for sensing, scanned probe and very high-frequency applications. *Nature Nanotech.* **2**, 114–120 (2007).
 - ¹¹ Jensen, K., Kim, K. & Zettl, A. An atomic-resolution nanomechanical mass sensor. *Nature Nanotech.* **3**, 533–537 (2008).
 - ¹² Naik, A. K., Hanay, M. S., Hiebert, W. K., Feng, X. L. & Roukes, M. L. Towards single-molecule nanomechanical mass spectrometry. *Nature Nanotech.* **4**, 445–450 (2009).
 - ¹³ Armour, A. D., Blencowe, M. P. & Schwab, K. C. Entanglement and decoherence of a micromechanical resonator via coupling to a cooper-pair box. *Phys. Rev. Lett.* **88**, 148301 (2002).
 - ¹⁴ Marshall, W., Simon, C., Penrose, R. & Bouwmeester, D. Towards quantum superpositions of a mirror. *Phys. Rev. Lett.* **91**, 130401 (2003).
 - ¹⁵ Blencowe, M. Quantum electromechanical systems. *Phys. Rep.* **395**, 159 (2004).
 - ¹⁶ Schwab, K. C. & Roukes, M. L. Putting mechanics into quantum mechanics. *Physics Today* **58**, 36 (2005).
 - ¹⁷ Kippenberg, T. J. & Vahala, K. J. Cavity optomechanics: Back-action at the mesoscale. *Science* **321**, 1172 (2008).
 - ¹⁸ Aspelmeyer, M. & Zeilinger, A. A quantum renaissance. *Physics World* **21** (2008).
 - ¹⁹ Aspelmeyer, M. & Schwab, K. Focus on mechanical systems at the quantum limit. *New J. Phys.* **10**, 095001 (2008).
 - ²⁰ O’Connell, A. D. *et al.* Quantum ground state and single-phonon control of a mechanical resonator. *Nature* **464**, 697–703 (2010).
 - ²¹ Wilson-Rae, I. Intrinsic dissipation in nanomechanical resonators due to phonon tunneling. *Phys. Rev. B* **77**, 245418 (2008).
 - ²² Kiselev, A. A. & Iafrate, G. J. Phonon dynamics and phonon assisted losses in euler-bernoulli nanobeams. *Phys. Rev. B* **77**, 205436 (2008).
 - ²³ Zener, C. Internal friction in solids. i. theory of internal friction in reeds. *Phys. Rev.* **52**, 230 (1937).
 - ²⁴ Lifshitz, R. & Roukes, M. L. Thermoelastic damping in micro- and nanomechanical systems. *Phys. Rev. B* **61**, 5600 (2000).
 - ²⁵ Duwel, A., Candler, R. N., Kenny, T. W. & Varghese, M. Engineering mems resonators with low thermoelastic damping. *J. Microelectromech. Syst.* **15**, 1437–1445 (2006).
 - ²⁶ Vignola, J. F. *et al.* Effect of viscous loss on mechanical resonators designed for mass detection. *Appl. Phys. Lett.* **88**, 041921 (2006).
 - ²⁷ Karabacak, D. M., Yakhot, V. & Ekinci, K. L. High-frequency nanofluidics: An experimental study using nanomechanical resonators. *Phys. Rev. Lett.* **98**, 254505 (2007).
 - ²⁸ Verbridge, S. S., Craighead, H. G. & Parpia, J. M. A megahertz nanomechanical resonator with room temperature quality factor over a million. *Appl. Phys. Lett.* **92**, 013112 (2008).
 - ²⁹ Yasumura, K. *et al.* Quality factors in micron- and submicron-thick cantilevers. *J. Microelectromech. Syst.* **9**, 117–125 (2000).
 - ³⁰ Mohanty, P. *et al.* Intrinsic dissipation in high-frequency micromechanical resonators. *Phys. Rev. B* **66**, 085416 (2002).
 - ³¹ Southworth, D. R. *et al.* Stress and silicon nitride: A crack in the universal dissipation of glasses. *Phys. Rev. Lett.* **102**, 225503 (2009).
 - ³² Venkatesan, A. *et al.* Dissipation due to tunneling two-level systems in gold nanomechanical resonators. *Phys. Rev. B* **81**, 073410 (2010).
 - ³³ Unterreithmeier, Q. P., Faust, T. & Kotthaus, J. P. Damping of nanomechanical resonators. *Phys. Rev. Lett.* **105**, 027205 (2010).
 - ³⁴ Seoáñez, C., Guinea, F. & Castro Neto, A. H. Surface dissipation in nanoelectromechanical systems: Unified description with the standard tunneling model and effects of metallic electrodes. *Phys. Rev. B* **77**, 125107 (2008).
 - ³⁵ Remus, L. G., Blencowe, M. P. & Tanaka, Y. Damping and decoherence of a nanomechanical resonator due to a few two-level systems. *Phys. Rev. B* **80**, 174103 (2009).
 - ³⁶ Mattila, T. *et al.* A 12 MHz micromechanical bulk acoustic mode oscillator. *Sensors and Actuators A: Physical* **101**, 1–9 (2002).
 - ³⁷ Anetsberger, G., Riviere, R., Schliesser, A., Arcizet, O. & Kippenberg, T. J. Ultralow-dissipation optomechanical resonators on a chip. *Nature Photon.* **2**, 627–633 (2008).

- ³⁸ Eichenfield, M., Chan, J., Camacho, R. M., Vahala, K. J. & Painter, O. Optomechanical crystals. *Nature* **462**, 78–82 (2009).
- ³⁹ Cross, M. C. & Lifshitz, R. Elastic wave transmission at an abrupt junction in a thin plate with application to heat transport and vibrations in mesoscopic systems. *Phys. Rev. B* **64**, 085324 (2001).
- ⁴⁰ Park, Y.-H. & Park, K. C. High-fidelity modeling of MEMS resonators – Part I: Anchor loss mechanisms through substrate. *J. Microelectromech. Syst.* **13**, 238 (2004).
- ⁴¹ Photiadis, D. M. & Judge, J. A. Attachment losses of high Q oscillators. *Appl. Phys. Lett.* **85**, 482 (2004).
- ⁴² Bindel, D. S. & Govindjee, S. Elastic PMLs for resonator anchor loss simulation. *Int. J. Numer. Meth. Engng.* **64**, 789 (2005).
- ⁴³ Judge, J. A., Photiadis, D. M., Vignola, J. F., Houston, B. H. & Jarzynski, J. Attachment loss of micromechanical and nanomechanical resonators in the limits of thick and thin support structures. *J. Appl. Phys.* **101**, 013521 (2007).
- ⁴⁴ Graff, K. F. *Wave Motion in Elastic Solids* (Dover, New York, 1991).
- ⁴⁵ Groblacher, S. *et al.* Demonstration of an ultracold micro-optomechanical oscillator in a cryogenic cavity. *Nature Phys.* **5**, 485–488 (2009).
- ⁴⁶ Cole, G. D., Groblacher, S., Gugler, K., Gigan, S. & Aspelmeyer, M. Monocrystalline Al(x)Ga(1-x)As heterostructures for high-reflectivity high-Q micromechanical resonators in the megahertz regime. *Appl. Phys. Lett.* **92**, 261108 (2008).
- ⁴⁷ LaHaye, M. D., Suh, J., Echternach, P. M., Schwab, K. C. & Roukes, M. L. Nanomechanical measurements of a superconducting qubit. *Nature* **459**, 960–964 (2009).
- ⁴⁸ Cole, G. D., Bai, Y., Aspelmeyer, M. & Fitzgerald, E. A. Free-standing Al(x)Ga(1-x)As heterostructures by gas-phase etching of germanium. *Appl. Phys. Lett.* **96**, 261102 (2010).
- ⁴⁹ Cole, G. D. *et al.* Megahertz monocrystalline optomechanical resonators with minimal dissipation. In *Proc. IEEE Micro Electro Mechanical Syst.*, 847–850 (2010). 23rd Int. Conf.